Intrinsic anisotropy of strain rate sensitivity in single crystal alpha titanium

Zhen Zhang, Tea-Sung Jun, T. Benjamin Britton, Fionn P.E. Dunne

Department of Materials, Royal School of Mines, Imperial College London, London, SW7 2AZ, UK

Abstract

The room temperature intrinsic strain rate sensitivities (SRS) of basal and prismatic slip systems have been determined for the α (HCP) phase of a titanium alloy (Ti-6242), through coupled crystal plasticity modelling and micro-pillar compression experiments. Load-displacement data from displacement hold tests, in both experiment and simulation, have enabled determination of the rate-dependent slip rule within the crystal plasticity model. Slip system SRS has been obtained, via micro-pillars orientated for single basal and prismatic slip. Crystal plasticity modelling explicitly captures micro-pillar geometry, crystal orientation, as well as the stiffnesses of components of the experimental testing frame and sample mounting. Consideration of the stiffness of the adhesive and load frame is shown to be essential for extraction of the intrinsic rate-dependent material response, rather than the structural response, even in single phase micro-pillar compression experiments. We find that the intrinsic SRS of basal slip is stronger than that for prismatic slip. This finding has significant implications in understanding the anisotropic rate-dependent response of hexagonal materials applied extensively under extreme loading conditions.

Keywords: *single crystal, alpha phase, Ti-6242, anisotropy, intrinsic strain rate sensitivity, substrate, micropillar compression test*

1. Introduction

Metals are widely used in a range of high performance engineering applications, where their strength at different strain rates is important for safety and component life. For instance, titanium alloys are widely used in critical aero-engine components, which may undergo rate sensitive deformation during operation, often involving dwell fatigue. The accumulation of plastic deformation during these loading modes exhibits a significant impact on in-service life. In particular, the introduction of a time sensitive 'dwell' under load, akin to cruise during many flight cycles, has been shown in some alloys to reduce the number of cycles to failure for components by an order of magnitude or more (the so-called 'dwell debit') [1]. This motivates studies of the strain rate sensitivity (SRS) of titanium alloys to understand the dwell debit and ultimately to manage titanium alloy use in aero-engine components more effectively.

Understanding materials performance in these complex loading modes is difficult, as both the stress state and microstructure are typically complex. It is therefore essential to extract out the intrinsic properties of individual phases, which allows the possibility of a direct and fair comparison of different alloy designs. Unfortunately, access to the performance of individual microstructural constituents is challenging, as often the growth of large single crystals is impossible from most engineering alloy systems with complicated microstructures. The advent of micro-pillar compression, where mechanical tests are conducted within a single grain, has spawned new possibilities of accessing materials properties of individual phases and grains. However, use of these properties for engineering at the larger scale requires some care, as the geometry and size of samples may play a role in the dislocation physics and these 'test geometry' effects (such as sample geometry, size and test frame) may control the apparent micromechanical response if they are not properly accounted for.

In practice, extracting engineering properties using micro-pillar compression is rather difficult. For instance, the presence of a size effect [2-6] makes extraction of pragmatic properties from pillars less than ~1μm in size very difficult. However, with care it is possible to understand the micromechanics of each test to extract intrinsic properties from extrinsic micromechanical performance [7]. The particular advantage of micro-pillar compression is that isolation of single crystal behaviour from that of the polycrystal is possible, when pillars are machined within individual grains often using focused ion beam machining [8, 9]. In practice, many micro-pillar compression tests are performed on pillars with sizes greater than 1 μm [10]. The aspect ratio of these pillars is selected to limit friction and buckling effects during compression, often ranging from 2:1 to 4:1 [11].

The majority of micro-pillar compression studies have been focused on cubic materials, such as Ni and Ni-based superalloys [12], Cu [13], Mo [14], and Au [4, 15]. Recent work has been extended to hexagonal-close-packed (HCP) metals, which have strong material elastic and slip anisotropy, and experiments show that anisotropy in size effects are found in single crystal magnesium (AZ31) pillars, with diameters between 0.3 μm and 5 μm [16]. Micro-pillar compression tests in prismatic titanium micro-pillars loaded along $[11\bar{2}0]$ showed that flow stress increases significantly with decreasing pillar size down to 300 nm [17]. The stress required for deformation twinning, $\{11\bar{2}2\}<\bar{1}\bar{1}23>$ and $\{10\bar{1}1\}<\bar{1}012>$ twinning system under [0001] compression, also increases greatly with decreasing sample size of a titanium alloy (Ti–5 at.% Al) single crystal, until the sample size is reduced to one micrometre [18]. Deformation twinning has not been found to occur in single crystal micro-pillar compression tests on magnesium, when compression was imposed along the $[0001]$ *c*-axis [19, 20].

Moving beyond yield, micro-pillar compression has also been used to explore deformation rate sensitivity. Recent experiments by Zhang et al. [21] investigated room temperature strain

rate sensitivity in single and polycrystalline Cu by deformation controlled stress relaxation tests of cylindrical pillars with diameters from 500nm to 1200nm. The strain rates considered ranged from 2×10^{-4} to 2×10^{-2} s^{-1} with strains up to 30% and results showed that grain boundaries may significantly suppress the strain bursts, which are observed in single crystal Cu micro-pillars. Choi et al. [22] performed uniaxial creep experiments on Ni pillars, with diameters of 600, 1000, and 2000 nm at room temperature. During the creep testing, the load was increased up to the desired maximum stress level (i.e. 400, 600, 800, 1000 MPa, respectively) at a fixed loading rate, $(\mathrm{d}P/\mathrm{d}t)/P = 0.05$ /s, then held for 200 s, and then unloaded at the same rate as the loading stage. It was found from the stress exponent and the activation volume for nanoscale creep under low stresses may be dominated by diffusion-controlled mechanisms. Gu and Ngan [23] studied the creep behaviour of precipitate-hardened duralumin (aluminium alloy 2025) micro-pillars. The pillars, with a diameter from 1 μm to 6.5 μm, were investigated by compression experiments at room temperature. The steady-state creep rate was found to be proportional to the lifetime of mobile dislocations, which rises with specimen size in the micron range due to the fact that the dislocations were not easily pinned in this range. Interestingly, they found that bi-crystalline pillars crept at a higher rate than the single crystals. TEM examination of the deformed microstructures suggested that the creep rate depends on the residual dislocation density.

This manuscript focuses on titanium alloys, as used in fan blades and discs for aero-engines. Titanium alloys are known to creep and show strong stress relaxation behaviour at low (~20°C) temperatures [24]. The creep behaviour of these alloys is thought to be influenced by the microstructure [25] and room temperature creep can lead to significant load shedding [26]. Load shedding is the phenomenon where progressive slip within a soft grain, due to creep for instance, results in increases in stress on a neighbouring hard grain. This is

believed to be a significant factor involved in the dwell debit during cold dwell fatigue of aero-engine discs [1, 27].

Systematic studies of creep and stress relaxation have been carried out on large single colony Ti alloys at millimetre scale by Mills et al. [28-32] which have revealed the complexity of the 'structural' deformation taking place by virtue of the kinematic constraint imposed on the development of α (HCP) slip by the adjacent β (BCC) ligaments which ordinarily satisfy the Burgers Orientation Relationship (BOR). α slip was found predominantly to contribute to the deformation, with β ligaments acting to block <a> type α slip. Both time-dependent creep deformation and stress relaxation were found to occur within the α phase, but not so in the β, for which little evidence of slip was observed. A recent review paper [33] summarises this work including the roles of short range order and tension-compression asymmetry in influencing the α slip observations. The BOR (determining the β orientation with respect to the α phase), and orientation of the α phase with respect to loading were found to have strong influence on α slip activation, creep behaviour, blocking of slip at α-β interfaces, and stress relaxation. These phenomena, and particularly the creep and stress relaxation, are likely to be crucial in determining the establishment of local dislocation activity and structure, pile-ups and resulting residual stress distributions, all of which are potentially important in subsequent defect nucleation and cold dwell fatigue debit.

We hypothesise that the well-known anisotropy of slip strength which exists for Ti alloys may also occur for the individual slip system strain rate sensitivities. Some evidence exists to support this; for example Inui et al. [34] found the strain rate sensitivity in Ti-56 at.%Al single crystal, a gamma-Ti-Al alloy, to be higher in $[\bar{1}52]$-oriented crystals than those oriented for $[021]$ slip between 150°C to 780°C. This tendency of strain rate sensitivity reversed in these two orientations from 800°C to 1000°C. Spitzig and Keh [35] also found

crystal-orientation dependent strain rate sensitivity in single crystal iron from -196°C to 22°C over strain rate range 5.6×10^{-4} s^{-1} to 2.8×10^{-3} s^{-1}.

There remain some experimental concerns with respect to micro-pillar tests which must be properly addressed if intrinsic properties are to be measured (especially for rate sensitive behaviour, where strain and stress vs time are important). These include the loading system stiffness which may, for example, be addressed for micro-pillar deformation tests with appropriate calibration [36]; the sample base stiffness, and that associated with the supporting substrate which is often used to mount the test samples within the loading frame. It has also been observed that the base material beneath the pillar under test can lead to an underestimation of the Young's modulus of the tested materials [37]. These effects must be accounted for if intrinsic properties, such as slip system strain rate sensitivity, are to be extracted.

The purpose of this study is to address strain rate sensitivity in single crystal near-α Ti-6242, using micro-pillar compression testing combined with crystal plasticity modelling. The focus is on measuring slip-system dependence of rate sensitivity. By utilising integrated experimental and crystal plasticity modelling of micro-pillar tests, the individual intrinsic basal and prismatic slip system rate sensitivities are extracted. Care within the modelling has been taken to fully account for the pillar substrate and loading machine stiffness to extract intrinsic material response. In addition, the inhomogeneous slip fields developed in the experiments with pillars with differing crystallographic orientation and slip activations are compared with those predicted from crystal plasticity modelling providing a thorough assessment of the model capabilities.

2. Material preparation, micro-pillar fabrication and compression test methodology

A 20mm diameter forged bar of Ti-6Al-2Sn-4Zr-2Mo (wt%) was obtained from IMR (Institute of Metal Research, China) as in reference [38]. Samples were taken from the bar sectioned perpendicular to its axis, and heat treated by holding the temperature at the beta transus + 50º (i.e. 1040ºC) for 8 hours, and cooling at a rate of 1ºC/min. This provides samples with large α lamellae separated by thin β ligaments, in clear prior β grain structures, which facilitates easy fabrication of (single crystal, single α phase) micro-pillars. The sample microstructure given in Figure 1 is from an electron-backscatter diffraction (EBSD) map, presented with orientations reported with respect to the sample surface normal (the loading axis for subsequently manufactured micro-pillars). Two regions highlighted as A2 and A3 in the map were chosen for pillar fabrication, where A2 and A3 are preferentially oriented to activate <a> type basal and prism slip respectively in single slip. Within each of these regions, single crystal α phase micro-pillars were made using focused ion beam machining, with custom scripts for consistent pillar machining, and further details can be found in [39]. The pillar dimensions are given in Table 1.

A total of four pillars (Table 1) have been selected from the two regions of α colonies in the Ti-6242 sample. Micro-pillar compression tests were carried out with two (nominal) strain rates of 1×10^{-2} and 2×10^{-3} s^{-1}. These strain rates have been achieved by controlling the displacement rate applied to each pillar taking account of the small variations in initial pillar height. Dimensions and crystallographic orientations for the α single-crystal fabricated pillars are given in Table 1. The global coordinate system is chosen to be consistent with the coordinate system adopted in the modelling work later. The detailed dimensions for each pillar may differ slightly compared to the pre-designed 2 μm wide (at the

top) and 5 μm in height. The small variations in taper angle Θ of the pillars may be attributed to the FIB sputtering process during milling [40, 41].

As shown in the schematic in Figure 2(a), each micro-pillar sits on its titanium matrix base which is mounted on the testing frame with a cyanoacrylate-based glue substrate. Displacement of the top pillar face downwards is performed using a diamond flat punch, compressing the pillar in displacement control. With pillars fabricated within the A2 region, the anticipated basal slip plane activation is indicated by the red shaded area in Figure 2(b) and the slip direction is illustrated by the red arrow. This is also demonstrated in Figure 2(c) for A3 pillars for which prismatic slip is anticipated.

Figure 3 shows the slip onset for two pillars for which basal slip is anticipated, i.e. A2P15 and A2P19 taken from the same A2 region. The images of the two pillar front views are given in Figure 3(a) and Figure 3(b), respectively. Observed slip lines are marked by green and white lines on the surfaces. Representative pole figures are shown in Figure 4. The applied loading is along the *Y*-direction which is the same as that shown in Figure 2.

Strain rate sensitivity and stress relaxation tests are carried out on the micro-pillars at differing strain rates. Expected profiles of strain vs time and stress vs time for displacement controlled loading, with a hold at peak displacement, are shown schematically in Figure 5(a & b). During the strain hold period, the pillar experiences stress relaxation resulting in a measured stress drop. For materials with positive strain rate sensitivity, such as titanium alloys, increasing strain rate leads to a greater flow stress.

The experimentally obtained stress-time curves for the tested pillars are given in Figure 6 for the strain rates indicated. A2 (basal slip) and A3 (prism slip) pillars have been (nominally) strained to 5% and 10% compressive strain, respectively. For ease of illustration, the time axis is normalized with respect to individual total loading time, including the additional one-

minute dwell time (time for stress relaxation at fixed displacement), at peak displacement. The nominal stress is calculated from the measured applied force and the mean pillar cross-sectional area, which is used both for experiment and simulation. It is found that during the displacement hold period there is stress relaxation, and the gradients of the stress-time curves for pillar A2P15 and A2P19 basal slip in Figure 6(a) are similar. This suggests the dislocation-governed deformation mechanisms under the two different strain rates operate equivalently. Similar behaviour is observed for prism slip in pillar A3P8 and A3P10 in Figure 6(b) except that the magnitude of the stress gradient can be seen to be lower than that for basal slip. In addition, the smaller separation of the stresses for the two strain rates shown for the prism slip pillar indicates that the strain rate sensitivity in this system is different to that for basal slip, and intuitively, basal slip appears to be more rate sensitive than prismatic slip.

Note that the nominal stress vs time responses for the differing pillars and strain rates shown in Figure 6 are determined by a remote load cell mounted below the sample and in series with the load-frame, sample and sample mount (as indicated in Figure 2). The experiment is designed to measure the pillar response, but the overall experimental force-time response is also affected by: (i) the titanium alloy base, from which the pillar was cut, which is chosen to be large compared with the pillar area to minimise effects (though substrate punch-in is expected), (ii) the glue substrate which potentially contributes significantly to the measured response (as it is significantly less stiff than the titanium pillar and base), and whose elastic properties need to be determined, and (iii) the overall loading machine response (including fixture of the sample stub) whose contribution, though likely to be small, is not neglected. It is necessary to establish, and account for, each of these stiffness contributions, and this necessitates the use of integrated crystal modelling which is introduced in the next section.

3. Micro-pillar crystal modelling methodology

Strain rate sensitivity is normally anticipated to become significant for homologous temperatures (T/T_m) in excess of about 0.3. The near-alpha titanium alloy considered in this paper, and similarly to other Ti alloys, [42, 43], clearly shows strong rate sensitivity even at 20°C and below [33]. There is much experimental evidence for the rate sensitivity, including room temperature creep and stress relaxation [28-30, 32, 44], but the mechanistic basis has not yet been fully established. There is no clear (e.g. TEM) evidence for dislocation climb mechanisms operating.

It is therefore argued that the strong rate sensitivity observed in Ti-6242 at low temperature is thermally activated and that it originates from the rate controlling process of combined obstacle pinning of dislocations together with thermally activated escape. Figure 7(a) shows schematically a dislocation gliding on its slip plane and becomes pinned by an array of obstacles. A thermal activation event under the applied shear stress τ enables the dislocation to attempt to overcome the energy barrier and escape the obstacles. The work carried out by the applied stress in driving the dislocation escape is $\tau\Delta V$, in which the activation volume ΔV can be calculated from the area A developed by the dislocation segment and the magnitude of Burgers vector, i.e. $\Delta V = Ab$. With the approximation that $d \approx b$, the activation volume may be expressed as $\Delta V = l_{obs}b^2$. The Gibbs free energy under the stress field, shown in Figure 7(b) is then given by

$$\Delta G = \Delta F - \tau\Delta V \tag{1}$$

which determines the energy barrier required to be overcome in order to induce thermally activated dislocation escape. The frequency of successful jumps to escape obstacles of only

forward activation was first introduced by Gibbs [45] and subsequently utilised by Dunne [46] considering both forward and backward activation events to give

$$\Gamma = \nu \exp\left(-\frac{\Delta F}{kT}\right)\sinh\left(\frac{\tau \Delta V}{kT}\right) \tag{2}$$

where ν is the frequency of attempts (successful or otherwise) of dislocations to jump the energy barrier, ΔF the activation energy, k the Boltzmann constant, and T the temperature. The crystal plasticity slip rule for activated system α is obtained from this by invoking the Orowan equation and is given by [46]

$$\dot{\gamma}^{\alpha} = \rho_m \nu b^2 \exp\left(-\frac{\Delta F}{kT}\right)\sinh\left[\frac{(\tau^{\alpha} - \tau_c^{\alpha})\Delta V}{kT}\right] \tag{3}$$

where ρ_m is the density of mobile dislocations, τ^{α} the resolved shear stress for the α^{th} slip system, and τ_c^{α} is the corresponding critical resolved shear stress (CRSS). In particular, ΔF is the activation energy for pinned dislocation escape, governing the overall time-sensitive deformation, i.e. creep behaviour. Note that the activation volume may be expressed as $\Delta V = \frac{\gamma_0 b^2}{\sqrt{\rho_o}}$, determining the length scale involved in thermodynamic diffusion processes, where ρ_o is the overall obstacle density, and γ_0 is the representative shear strain magnitude which influences the transient creep response.

In this study, single crystal α phase Ti pillars in Ti-6242 are considered and all pillars are chosen to be (approximately) of the same size and do not contain internal interfaces. Hence it is reasonable to discard the contribution of geometrically necessary dislocations ρ_{GND} and this enables reasonable comparative assessment between pillars. Independent single crystal tests indicate very little strain hardening so that the hardening effect due to statistically stored

dislocations ρ_{SSD} is anticipated to be small. However, the overall obstacle density ρ_o in calculating ΔV is simply taken to be ρ_{SSD} because ρ_{GND} is small.

The model is adopted to extract the critical resolved shear stresses τ_c^α for basal and prismatic slip systems, using different pillars oriented for single slip. This methodology is presented fully in a later section. For pyramidal $< c + a >$ slip, the critical resolved shear stress in the crystal model is taken from other work to be three times that for prismatic slip [47]. As tests were performed at different strain rates and with a displacement hold, the model was calibrated by varying (in addition to τ_c^α) both the activation energy ΔF and the reference shear strain γ_0. All other parameters are fixed and are defined later in Table 2. This brief crystal model description is completed by noting that the slip rule defined in Eq. (3), within the crystal plasticity formulation, is coded into ABAQUS in terms of a three-dimensional 20-noded quadratic user-defined finite element (UEL).

The primary purpose of the crystal plasticity model is to enable the key intrinsic materials properties of the α-Ti single crystal pillars to be extracted. As the load-displacement response is measured remotely to the sample, these responses must be compared with a model that includes contributions from the indenter frame and substrate mounting as previously noted. In particular, we focus on including contributions from the cyanoacrylate-based glue substrate, the titanium base and the load frame as elastic isotropic layers loaded in series with the pillar. These transpire to be crucially important for the determination of strain rate-sensitivities. The mesh sensitivity of the pillar model is also examined in the context of the extraction of the required pillar mechanical properties. In order to carry out these preliminary modelling studies, representative material properties for the α phase of Ti-6242 are required and are given in Table 2, and have been obtained either from within the present study, or from independent literature where necessary.

3.1 Establishment of non-pillar contributions to load-displacement test data

The experimental pillar samples are machined from singe crystal α colonies of Ti-6242, and are located upon a substantial Ti base, as shown schematically in Figure 2, and in actuality in Figure 3. The base titanium material under the pillar potentially imposes lateral confinement on the pillar under compression as well as compliance due to 'punch in', and in our pillar modelling studies the Ti base is explicitly included. The (single crystal) pillar properties are taken to be those given in Table 2, and the (polycrystal) Ti-6242 base is reasonably taken to be elastically isotropic.

Micro-pillar test behaviour is often obtained from remote measurement from a load cell and displacement from the applied actuation of the flat punch within the loading frame. A consequence is that the recorded response often comprises pillar deformation combined with displacement of the substrate (if present) together with a contribution from the loading machine compliance. The experiments conducted here utilise the loading rig shown in Figure 8(a) and represented schematically in 8(b). The pillar is cut from bulk and therefore includes a Ti base which is mounted on to the load cell by means of a cyanoacrylate-based glue substrate of finite thickness. The titanium base is reasonably assumed to be elastically isotropic, and to behave differently to the anisotropic elastic and plastic response of the pillar. The cyanoacrylate-based glue behaves elastically with a modulus considerably smaller than that for the titanium pillar and base, but a guidance value only for its modulus is known from the manufacturer. Because of the serial loading applied (through pillar, base, glue substrate and machine loading column), and from the linearity of elasticity, the elastic stiffness contributions from the base (k_{base}), glue substrate (k_{glue}), and loading column (k_{col}) may be combined to give an effective (henceforth termed environmental) stiffness k_{env}, given by

$$\frac{1}{k_{env}} = \frac{1}{k_{base}} + \frac{1}{k_{glue}} + \frac{1}{k_{col}} \tag{4}$$

The overall laboratory force (F) – displacement (u^e) response, measured early in the loading and therefore while all pillar deformation is elastic, may then be expressed

$$F = \frac{1}{\frac{1}{k_{env}} + \frac{1}{k_{pillar}}} u^e \tag{5}$$

where k_{pillar} is the pillar elastic stiffness and k_{env} given by equation (4). The elastically anisotropic moduli of the pillar and the isotropic modulus of the titanium base are known so that k_{pillar} and k_{base} are also known. The environmental stiffness, k_{env}, is determined directly using the crystal pillar CPFE representation shown in Figure 9(a) in which the pillar is shown together with the effective base which is assigned an elastic modulus to give the resulting stiffness k_{env} in order to replicate the experimental pillar elastic load – displacement response shown in Figure 10(b) for pillar A3P8. For comparison, the resulting predicted load – displacement responses obtained for the case in which neither the Ti base nor glue substrate are included, and the case for which the glue substrate is excluded, show the importance of their inclusion in ensuring pillar displacements are accurately captured, as also discussed in [37]. The effective modulus corresponding to the environmental stiffness is found to be $E_{env} \approx 7$ GPa from Figure 9(b), and it is noted that the modulus range for cyanoacrylate based adhesive published by the manufacturer is 3 GPa to 15 GPa [48, 49] indicating that the effective stiffness is dominated by that of the glue substrate.

3.1.1 Effect of environmental stiffness on stress relaxation observations

It transpires that the correct representation of the non-pillar stiffness contributions to the measured response is equally important in relation to the extraction of pillar strain rate sensitivity properties because of their effects on apparent stress relaxation. Consider the total displacement of the indenter to be h consisting of the contributions from material within the pillar and all non-pillar compliance (e.g. glue, frame and substrate) so that it may be expressed

$$h = u_{env} + u^{e}_{pillar} + u^{p}_{pillar} \tag{6}$$

where u_{env} are the displacements from all non-pillar contributions, and u^{e}_{pillar} and u^{p}_{pillar} the elastic and plastic pillar deformations, respectively. The object is loaded in series and therefore each load-bearing member carries the same force, F, so that Eq. (6) may be re-written in rate form in terms of this force and the key stiffness terms as

$$\dot{h} = \frac{\dot{F}}{k_{env}} + \frac{\dot{F}}{k_{pillar}} + \dot{u}^{p}_{pillar} \tag{7}$$

in which k_{env} and k_{pillar} are defined above. Rearranging Eq. (7) gives

$$\dot{F} = \frac{k_{pillar}}{\left[1 + k_{pillar} \big/ k_{env}\right]} (\dot{h} - \dot{u}^{p}_{pillar}) \tag{8}$$

where the rate of pillar plastic displacement $\dot{u}^{p}_{pillar}$ is controlled by the slip rate from activated slip systems, and determined from the crystal plasticity model. which may be expressed in incremental form to give load drop e.g. resulting from stress relaxation, in terms of displacement changes by

(9)

$$\Delta F = \frac{k_{pillar}}{1 + \frac{k_{pillar}}{k_{env}}} (\Delta h - \Delta u^{p}_{pillar})$$

Under purely linear elastic deformation (i.e. by setting $\Delta u^{p}_{pillar} = 0$), it is seen from Eq. (9) that the environmental stiffness affects the measured elastic stiffness (as discussed above). When plasticity is included, Eq. (9) shows that the non-linear stress relaxation which occurs may be strongly affected by the non-pillar stiffness terms modifying the magnitude of the stress drop. Hence, measured stress relaxations from the pillar and the non-pillar contributions must be accounted for. Figure 10 shows the CPFE calculated (nominal) stress response with time when the environmental stiffness is and is not included in the calculations, again making clear that the overall pillar experimental measurements of stress relaxation contain contributions from the pillar response and that from the substrate which need to be distinguished. Particularly, in the context of rate sensitivity measurements from pillars, it is clear that strain rate sensitivity properties of the underlying pillar single crystal material may be incorrectly determined if the environmental stiffness is neglected. In passing, note that the crystal model properties used in Figure 10 are those used consistently throughout this study and in fact have been determined from the pillar tests presented in this paper, the details of which are presented in Section 4. Note also that the effective stiffness from the cyanoacrylate-based glue substrate, titanium base and loading machine has been explicitly included in all subsequent modelling to ensure their behaviours are included and distinguished from those of the micro-pillar itself.

3.2 Convergence study for crystal plasticity model

The section on micro-pillar crystal modelling methodology is completed by considering a finite element mesh convergence study with respect to the micro-pillar representation. This is

to ensure that the finite element model can appropriately account for the non-uniform stress state due to the taper and constraints imposed, as well as the substrate effects in the micro-pillar compression tests. A finite element study has been conducted to determine the size of substrate and pillar base region shown in Figure 9(a). It is found that it is appropriate to model a cubic substrate and base with height five times that of the pillar base size. In this case, the stresses at the outer surface of the cubic supporting block are negligibly small and the fixed boundary condition at bottom of the block will have negligible influence on the stress relaxation. Figure 11 shows the micro-pillar nominal stress response to the displacement loading schematically shown in Figure 5 including the stress relaxation during the displacement hold. The FE model containing 432 elements in the micro-pillar giving a mesh with a total of 1687 elements in fact gives results almost identical to those resulting from four times more elements. In addition, the study has been extended to address the time step size selection to ensure the non-linear plastic and rate-dependent stress relaxation behaviour is appropriately captured with adequate but economical step size.

4. Crystal plasticity model analysis and integration with experiments

We now address fully integrated micro-pillar test and crystal plasticity modelling in order to investigate slip strength, slip system strain rate sensitivity, and pillar stress relaxation in single α phase, from the near α alloy Ti-6242 at 20°C in which differing basal and prismatic slip systems are activated. The finite element crystal plasticity micro-pillar model is shown in Figure 9(a) in which the pillar and the titanium base and substrate are modelled with about 1700 user-defined 20-noded elements.

The correct model representation of the experimentally observed crystal orientation is crucially important in studying rate sensitive behaviour in micro-pillar tests as will become

clear. The model is established with knowledge of crystal orientation and anisotropic elastic moduli. Within the constitutive rule, there are three independent crystal model parameters to be determined: the activation energy, ΔF^{α}; the activation volume parameter, γ_0^{α}; and the slip system strength τ_c^{α}.

The activation energy and activation volume parameters describe in the model the rate sensitivity which includes, for example, stress relaxation behaviour (with ΔF^{α} and γ_0^{α} determining the time constant associated with the stress drop), and have in all previous work been deemed to be slip-system independent. The new experimental findings presented above indicate that basal and prismatic slip systems for Ti-6242 show rate sensitive behaviours which are empirically different. Hence, we keep open the possibility that as a consequence, ΔF^{α} and γ_0^{α} may be slip-system dependent. This is compatible with the findings of May [50] who also observed differing slip system rate sensitivities in strain-rate controlled uniaxial tests on appropriately orientated single crystals.

All other crystal plasticity parameters in Eq.(3) are as reported elsewhere [46, 51] and are given in full in Table 2. Calibration of the model is completed by considering the stress relaxation experimental results for A2 (basal slip) and A3 (prismatic slip) micro-pillars shown in Figure 12 combined with crystal plasticity modelling in order to determine parameters ΔF^{α}, γ_0^{α}, and τ_c^{α} for basal and prismatic slip to reproduce the experimentally measured pillar stress relaxation and the results are reported in Table 2. The elastic anisotropic properties are given in Table 3.

Mobile dislocation densities in commercially pure Ti have been cited between 10^{10} to 10^{16} m^{-2} in the literature [52]. Nemat-Nasser, Guo and Cheng [52] took a density of 10^{13} m^{-2} in their study which is similar to that utilised here in Table 2. In addition, Ashby [53] showed

the magnitude of initially stored dislocation density to be around 10^{10} m^{-2} to 10^{11} m^{-2} for a single crystal copper sample. It can also be deduced from Kirane and Ghosh [54] that they assume an initially stored dislocation density of about 10^{9} m^{-2} in their work on a Ti alloy. These works show that the initial stored dislocation density $\rho_o = 10^{10}$ m^{2} utilised in this work is certainly compatible with other studies.

The activation volume is given by $\Delta V = \frac{\gamma_0 b^2}{\sqrt{\rho_o}}$ in the crystal slip rule, such that the parameters in Table 2 give ΔV =1.2 b^3 for basal slip and 12 b^3 for prismatic slip systems. These are close to the lower bound of the range for alpha titanium at low temperature (T<0.4Tm), given by Conrad [55] to be between about 8b^3 and 80b^3, but it is noted that the data given in [55] were obtained by consideration of macro-scale polycrystal samples. In the present work, our focus is on single crystal, single phase alpha Ti, and differences are therefore anticipated. The rate sensitivity resulting from an activation volume ΔV may also be indirectly assessed against structural strain rate sensitivity *m*, defined as $m = \frac{\partial \ln \sigma}{\partial \ln \dot{\varepsilon}}$, which has been found to be inversely proportional to the activation volume [56-58]. This not only reflects our findings that both basal and prismatic systems are rate dependent (at the strain rate regime considered), but also that basal slip systems are more sensitive than the prismatics.

Kocks, Argon and Ashby [59] pointed out that when $\Delta F > kT$, the Arrhenius rate equation i.e. $\nu = \nu_0 \exp\left(-\frac{\Delta F}{kT}\right)$ (where ν and ν_0 are the probability of dislocation jumps over obstacles and the reference probability, respectively) is applicable for representing the rate of thermal activation and in the present work, $\frac{\Delta F}{kT}$ is found to be 17 for basal slip and 22 for prismatic slip systems. Thermally activated dislocation escape is the basis for the establishment of the slip rule to capture the strongly rate-sensitive behaviour of alloy Ti-6242, as discussed in Section 3 of the paper. The case of low stress, which is sometimes of less practical interest,

leads to the growing significance of dislocation back jumps [59], which are potentially important for low-temperature, low-stress creep of relevance to dwell fatigue in titanium alloys. In these alloys, creep may occur even when the stress is below yield [60]. The slip rule detailed in Section 3 explicitly incorporates both forward and backward activation events and is therefore appropriate for the low-temperature, low-stress creep regime in addition to that for higher stresses where forward dislocation escape predominates.

The resulting comparison between crystal model calculated and experimentally measured micro-pillar (nominal) stress – time, and stress – strain responses for single-crystal basal (A2P15) and prismatic (A3P19) slip are shown in Figure 12. Note that the nominal pillar stress is calculated from the force (in experiment from load cell) and the mean pillar cross-sectional area. This is accordingly implemented in the model. Strain is determined from the displacement of the indenter divided by the original pillar height. The calculated results show reasonable agreement with the experiments both in terms of transient stress drop and overall rate of stress relaxation from the stress-time curves in Figure 12. The differing stress-strain responses for the two micro-pillars for basal and prismatic slip are also found to be well represented by the model in Figure 12.

In addition to good agreement in overall stress-time, stress-strain behaviours in Figure 12, a detailed comparison is presented of the observed and predicted micro-pillar slip responses as illustrated in Figure 13 (for basal slip) and Figure 14 (for prism slip). The predicted crystal slip activity from crystal plasticity modelling shows very good agreement with the experimental basal-activated A2 pillars, particularly in terms of the intersections of slip planes with the four pillar free surfaces. The calculated results shown in colour represent the accumulated slip along the $(0001)[\bar{2}110]$ system in Figure 13 (for basal slip), and along slip system $(10\bar{1}0)[\bar{1}2\bar{1}0]$ in Figure 14 (for prism slip).

It may be seen from pillar A3P8 in Figure 14 that model predicted slip shows reasonable agreement with the experimental observations. Note that there are parallel zones of prismatic slip developed in the A3 pillar experiment, which are not immediately obvious in the predicted slip fields shown. For the former, the first slip plane nucleates from the top left corner in the back view (b) in the experiment. The slip direction follows $(10\bar{1}0)[\bar{1}2\bar{1}0]$, and this slip nucleation occurs due to the stress localization at the top corner where the indenter contacts the pillar. The general good agreement between model and micro-pillar tests including the localization of slip and its 3D development in the pillars with differing crystallographic orientations and slip system activity, together with reasonable representation of the rate-sensitive and stress relaxation pillar responses, is very encouraging.

It is noted that the micro-pillar tests described above and used in order to identify key model parameters were carried out at nominal strain rate of $1\times10^{-2}\ s^{-1}$. We further utilise the crystal plasticity model to blind predict the experimental micro-pillar tests carried out at a strain rate of $2\times10^{-3}\ s^{-1}$, and the comparison of results is shown in Figure 15. Again, good agreement in (nominal) stress – strain behaviour is obtained, and also for the experimental and predicted micro-pillar stress relaxations for both pillar A2P19 (for basal slip) and A3P10 (for prismatic slip).

4.1 Basal slip system has stronger strain rate sensitivity than prismatic slip system

It is interesting to note that the basal and prismatic systems have different intrinsic strain rate sensitivities. This is quantified by the differences in ΔF and γ_0 (with the latter indicative of the activation volume) in Table 2 for the basal and prismatic systems, and we note that in

recognising the differing rate sensitivities, the crystal model captures correctly the experimental basal and prismatic micro-pillar rate-sensitive responses. The strain rate effect manifests itself as differing strain rate strengthening dependence, or in the differing stress relaxation responses.

The observation that the independent basal and prism slip systems possess differing strain rate sensitivities, with our observations and analyses indicating a stronger rate sensitivity in basal systems over prismatic, raises many interesting questions. These are associated with properties and performance of these alloys in service (e.g. in connection particularly with cold dwell fatigue for which rate-behaviour is argued by many to play a crucial role), but also in the context of generating opportunities to engineer microstructures for optimal rate-sensitivity to avoid detrimental properties. Many commercially-useful Ti alloys display strong rate-dependent behaviours (e.g. creep) as outlined in the introduction section.

In order to demonstrate the parameter sensitivity and anisotropic rate dependence of basal and prismatic slip systems, the basal rate-controlling properties (i.e. τ_c, ΔF and ΔV) in Table 2 are utilised to predict the prism pillar experimental response and similarly, the prism rate sensitivity in Table 2 is used to predict the experimental basal pillar response. Numerical results based on the exchanged rate sensitivity parameters are superimposed on the data given in Figure 12(a) and 12(c) and are shown (green broken lines) in Figure 16(a) for the basal slip pillar and (b) for the prism slip pillar. Due to the strong anisotropy and differences in the rate dependence of the two slip system types, quite different results are observed with failure to capture the experimental observations. The results reinforce the strength of the anisotropy and the need to recognise the differing intrinsic rate sensitivities of basal and prism slip in the Ti alloy studied.

Conclusion

Integrated crystal plasticity modelling of micro-pillar tests has been utilised to demarcate the contributions of micro-pillar, substrate and machine stiffness to the overall test force-displacement measurements in order to distinguish and extract out intrinsic behaviour of the pillar material. Micro-pillar compression stress relaxation tests on single crystal α alloy Ti-6242 at 20°C have shown that α phase basal and prismatic slip systems have differing strain rate sensitivities. The basal and prismatic slip strengths, and the rate sensitivities of basal and prismatic slip systems have been quantified. Rate-controlling activation energies for basal and prismatic slip systems are found to be 0.4247 ± 0.0002 eV (6.8048×10^{-20} J/atom) and 0.5621 ± 0.0002 eV (9.0068×10^{-20} J/atom) respectively.

The crystal plasticity modelling of the micro-pillars demonstrates that the differing stress relaxation behaviours resulting from basal and prismatic slip may be accurately captured and the strain rate effect predicted correctly. Slip development and localisation occurring within the experimental micro-pillar tests is also well reproduced by the crystal model. Using this combined experiment and computational approach for extraction of these properties using a crystal plasticity model also enables more complex microstructures and mechanical performance to be explored.

Acknowledgement

The authors gratefully acknowledge the Engineering & Physical Science Research Council for funding through HexMat (EP/K034332). Further details of the HexMat grant can be found at http://www.imperial.ac.uk/hexmat. TBB and FPED would like to acknowledge the Royal Academic of Engineering for additional funding for their Research Fellowship and Chair respectively. We would like to thank Giorgio Sernicola for assistance in fabricating and testing the micropillars.

References

[1] M.R. Bache, A review of dwell sensitive fatigue in titanium alloys: the role of microstructure, texture and operating conditions, *Int. J. Fatigue* **25**, 2003, 1079-1087.

[2] D. Kiener, P.J. Guruprasad, S.M. Keralavarma, G. Dehm and A.A. Benzerga, Work hardening in micropillar compression: In situ experiments and modeling, *Acta Mater.* **59**, 2011, 3825-3840.

[3] A.S. Schneider, C.P. Frick, B.G. Clark, P.A. Gruber and E. Arzt, Influence of orientation on the size effect in bcc pillars with different critical temperatures, *Mater. Sci. Eng. A* **528**, 2011, 1540-1547.

[4] J.R. Greer, W.C. Oliver and W.D. Nix, Size dependence of mechanical properties of gold at the micron scale in the absence of strain gradients, *Acta Mater.* **53**, 2005, 1821-1830.

[5] J.R. Greer and W.D. Nix, Nanoscale gold pillars strengthened through dislocation starvation, *Phys. Rev. B* **73**, 2006.

[6] T. Zhu, J. Li, A. Samanta, A. Leach and K. Gall, Temperature and strain-rate dependence of surface dislocation nucleation, *Phys. Rev. Lett.* **100**, 2008.

[7] J.R. Greer and J.T.M. De Hosson, Plasticity in small-sized metallic systems: Intrinsic versus extrinsic size effect, *Prog. Mater. Sci.* **56**, 2011, 654-724.

[8] J.R. Greer, Effective Use of Focused Ion Beam (FIB) in Investigating Fundamental Mechanical Properties of Metals at the Sub-Micron Scale, *MRS Proceedings* **983**, 2006, 0983-LL0908-0903.

[9] D.M.D. Michael D. Uchic, Jeffrey N. Florando and William D. Nix, Exploring specimen size effects in plastic deformation of Ni3(Al,Ta), *MRS Proceedings* **753**, 2002, BB1.4.1-BB1.4.6.

[10] O. Kraft, P.A. Gruber, R. Moenig and D. Weygand, Plasticity in Confined Dimensions, *Annu. Rev. Mater. Res.* **40**, 2010, 293-317.

[11] M.D. Uchic, D.M. Dimiduk, J.N. Florando and W.D. Nix, Sample dimensions influence strength and crystal plasticity, *Science* **305**, 2004, 986-989.

[12] C.P. Frick, B.G. Clark, S. Orso, A.S. Schneider and E. Arzt, Size effect on strength and strain hardening of small-scale 111 nickel compression pillars, *Mater. Sci. Eng. A* **489**, 2008, 319-329.

[13] A.T. Jennings, J. Li and J.R. Greer, Emergence of strain-rate sensitivity in Cu nanopillars: Transition from dislocation multiplication to dislocation nucleation, *Acta Mater.* **59**, 2011, 5627-5637.

[14] H. Bei, S. Shim, E.P. George, M.K. Miller, E.G. Herbert and G.M. Pharr, Compressive strengths of molybdenum alloy micro-pillars prepared using a new technique, *Scr. Mater.* **57**, 2007, 397-400.

[15] C.A. Volkert and E.T. Lilleodden, Size effects in the deformation of sub-micron Au columns, *Philos. Mag.* **86**, 2006, 5567-5579.

[16] Z.H. Aitken, H. Fan, J.A. El-Awady and J.R. Greer, The effect of size, orientation and alloying on the deformation of AZ31 nanopillars, *J. Mech. Phys. Solids* **76**, 2015, 208-223.

[17] Q. Sun, Q. Guo, X. Yao, L. Xiao, J.R. Greer and J. Sun, Size effects in strength and plasticity of single-crystalline titanium micropillars with prismatic slip orientation, *Scr. Mater.* **65**, 2011, 473-476.

[18] Q. Yu, Z.-W. Shan, J. Li, X. Huang, L. Xiao, J. Sun and E. Ma, Strong crystal size effect on deformation twinning, *Nature* **463**, 2010, 335-338.

[19] C.M. Byer, B. Li, B. Cao and K.T. Ramesh, Microcompression of single-crystal magnesium, *Scr. Mater.* **62**, 2010, 536-539.

[20] E. Lilleodden, Microcompression study of Mg (0001) single crystal, *Scr. Mater.* **62**, 2010, 532-535.

[21] J.Y. Zhang, G. Liu and J. Sun, Strain rate effects on the mechanical response in multi- and single-crystalline Cu micropillars: Grain boundary effects, *Int. J. Plasticity* **50**, 2013, 1-17.

[22] I.-C. Choi, Y.-J. Kim, M.-Y. Seok, B.-G. Yoo, J.-Y. Kim, Y. Wang and J.-i. Jang, Nanoscale room temperature creep of nanocrystalline nickel pillars at low stresses, *Int. J. Plasticity* **41**, 2013, 53-64.

[23] R. Gu and A.H.W. Ngan, Size-dependent creep of duralumin micro-pillars at room temperature, *Int. J. Plasticity* **55**, 2014, 219-231.

[24] H. Adenstedt, Creep of titanium at room temperature, *Met. Prog.* **56**, 1949, 658-660.

[25] G. Lutjering, Influence of processing on microstructure and mechanical properties of (alpha+beta) titanium alloys, *Mater. Sci. Eng. A* **243**, 1998, 32-45.

[26] V. Hasija, S. Ghosh, M.J. Mills and D.S. Joseph, Deformation and creep modeling in polycrystalline Ti-6Al alloys, *Acta Mater.* **51**, 2003, 4533-4549.

[27] F.P.E. Dunne and D. Rugg, On the mechanisms of fatigue facet nucleation in titanium alloys, *Fatigue Fract. Eng. M.* **31**, 2008, 949-958.

[28] M.F. Savage, J. Tatalovich and M.J. Mills, Anisotropy in the room-temperature deformation of alpha-beta colonies in titanium alloys: role of the alpha-beta interface, *Philos. Mag.* **84**, 2004, 1127-1154.

[29] S. Suri, G.B. Viswanathan, T. Neeraj, D.H. Hou and M.J. Mills, Room temperature deformation and mechanisms of slip transmission in oriented single-colony crystals of an alpha/beta titanium alloy, *Acta Mater.* **47**, 1999, 1019-1034.

[30] D. Deka, D.S. Joseph, S. Ghosh and M.J. Mills, Crystal plasticity modeling of deformation and creep in polycrystalline Ti-6242, *Metall. Mater. Trans. A* **37A**, 2006, 1371-1388.

[31] G. Venkatramani, S. Ghosh and M. Mills, A size-dependent crystal plasticity finite-element model for creep and load shedding in polycrystalline titanium alloys, *Acta Mater.* **55**, 2007, 3971-3986.

[32] T. Neeraj, D.H. Hou, G.S. Daehn and M.J. Mills, Phenonomenological and microstructural analysis of room temperature creep in titanium alloys, *Acta Mater.* **48**, 2000, 1225-1238.

[33] T.B. Britton, F.P.E. Dunne and A.J. Wilkinson, On the mechanistic basis of deformation at the microscale in hexagonal close-packed metals, *Proc. R. Soc. A* **471**, 2015, 20140881.

[34] H. Inui, M. Matsumuro, D.H. Wu and M. Yamaguchi, Temperature dependence of yield stress, deformation mode and deformation structure in single crystals of TiAl (Ti-56 at% Al), *Philos. Mag.* **75**, 1997, 395-423.

[35] W.A. Spitzig and A.S. Keh, Orientation dependence of the strain-rate sensitivity and thermally activated flow in iron single crystals, *Acta Metall.* **18**, 1970, 1021–1033.

[36] D. Kiener, C. Motz and G. Dehm, Micro-compression testing: A critical discussion of experimental constraints, *Mater. Sci. Eng. A* **505**, 2009, 79-87.

[37] I.-S. Choi, Y. Gan, D. Kaufmann, O. Kraft and R. Schwaiger, Measurement of Young's modulus of anisotropic materials using microcompression testing, *J. Mater. Res.* **27**, 2012, 2752-2759.

[38] T.-S. Jun, G. Sernicola, F.P.E. Dunne and T.B. Britton, Local deformation mechanisms of two-phase Ti alloy, *Mater. Sci. Eng. A* **649**, 2016, 39-47.

[39] T.-S. Jun, Z. Zhang, G. Sernicola, F.P.E. Dunne and T.B. Britton, Local strain rate sensitivity of single α phase within a dual-phase Ti alloy, *Acta Mater.* **107**, 2016, 298-309.

[40] L.A. Giannuzzi, Introduction to focused ion beams: instrumentation, theory, techniques and practice, 2006, Springer Science & Business Media; New York.

[41] C.A. Volkert and A.M. Minor, Focused ion beam microscopy and micromachining, *MRS Bull.* **32**, 2007, 389-399.

[42] G. Welsch, R. Boyer and E. Collings, Materials properties handbook: titanium alloys, 1993, ASM international.

[43] V.A. Joshi, Titanium alloys: an atlas of structures and fracture features, 2006, CRC Press.

[44] M.A. Imam and C.M. Gilmore, Room temperature creep of Ti-6AI-4V, *Metall. Trans. A* **10**, 1979, 419-425.

[45] G.B. Gibbs, Thermodynamic analysis of dislocation glide controlled by dispersed local obstacles, *Mater. Sci. Eng.* **4**, 1969, 313-328.

[46] F.P.E. Dunne, D. Rugg and A. Walker, Lengthscale-dependent, elastically anisotropic, physically-based hcp crystal plasticity: Application to cold-dwell fatigue in Ti alloys, *Int. J. Plasticity* **23**, 2007, 1061-1083.

[47] J. Gong and A.J. Wilkinson, Anisotropy in the plastic flow properties of single-crystal α titanium determined from micro-cantilever beams, *Acta Mater.* **57**, 2009, 5693-5705.

[48] K.W. Allen, Adhesion 12, 1984, Springer Verlag; New York.

[49] B. Ellis and R. Smith, Polymers: A Property Database, 2008, CRC Press; Florida.

[50] K. May. Master Thesis, Department of Materials Science and Engineering. Columbus, United States: The Ohio State University, 2010.

[51] Z. Zhang, M.A. Cuddihy and F.P.E. Dunne, On rate-dependent polycrystal deformation: the temperature sensitivity of cold dwell fatigue, *Proc. R. Soc. A* **471**, 2015, 20150214.

[52] S. Nemat-Nasser, W. Guo and J. Cheng, Mechanical properties and deformation mechanisms of a commercially pure titanium, *Acta mater.* **47**, 1999, 3705-3720.

[53] M. Ashby, The deformation of plastically non-homogeneous materials, *Philos. Mag.* **21**, 1970, 399-424.

[54] K. Kirane and S. Ghosh, A cold dwell fatigue crack nucleation criterion for polycrystalline Ti-6242 using grain-level crystal plasticity FE model, *Int. J. Fatigue* **30**, 2008, 2127-2139.

[55] H. Conrad, Thermally activated deformation of alpha titanium below 0.4 Tm., *Can. J. Phys.* **45**, 1967, 581-590.

[56] M.A. Meyers, A. Mishra and D.J. Benson, Mechanical properties of nanocrystalline materials, *Prog. Mater. Sci.* **51**, 2006, 427-556.

[57] Y. Wang, A. Hamza and E. Ma, Temperature-dependent strain rate sensitivity and activation volume of nanocrystalline Ni, *Acta Mater.* **54**, 2006, 2715-2726.

[58] Q. Wei, Strain rate effects in the ultrafine grain and nanocrystalline regimes - influence on some constitutive responses, *J. Mater. Sci.* **42**, 2007, 1709-1727.

[59] U.F. Kocks, A.S. Argon and M.F. Ashby, Thermodynamics and kinetics of slip, *Prog. Mater. Sci.* **19**, 1975, 1-281.

[60] R. Ankem and T. Wilt, A literature review of low temperature (< 0.25 Tmp) creep behavior of alpha, alpha-beta, and beta titanium alloys, *San Antonio, TX: Center for Nuclear Waste Regulatory Analyses*, 2006.

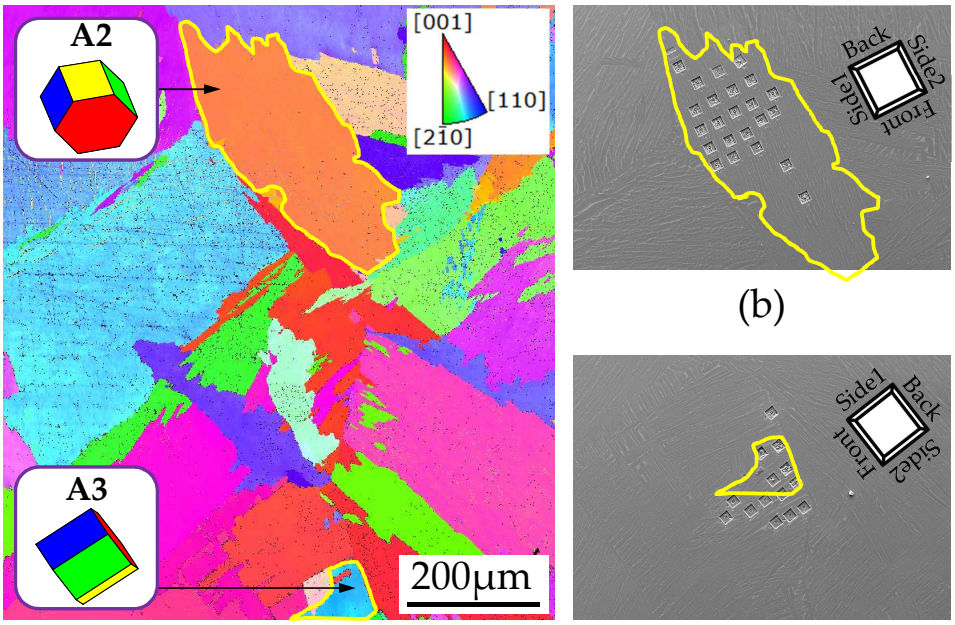


Figure 1: (a) Inverse pole figure map with respect to the surface normal, i.e. pillar loading direction, showing crystal orientations of α phase and target regions A2 and A3 chosen for pillar fabrication; (b-c) pillar extracted from A2 and A3 region with inserts indicating their four surfaces.

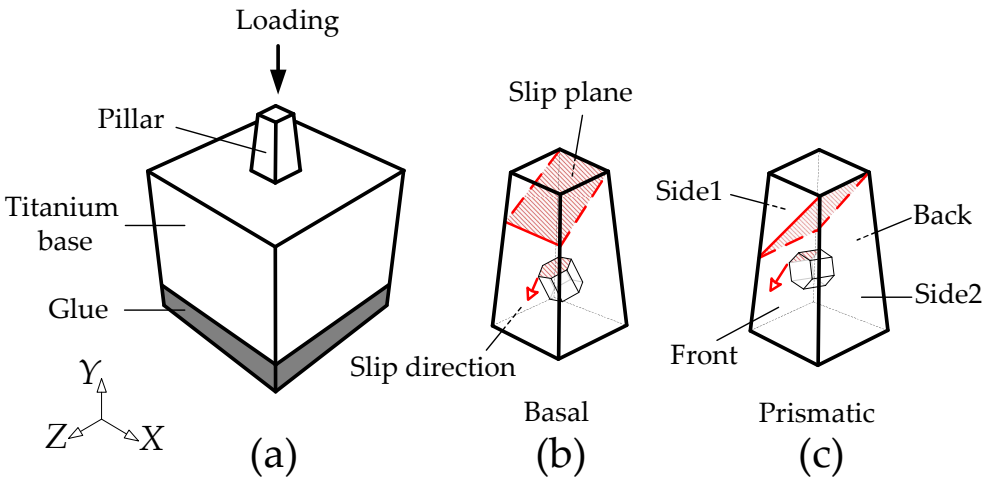


Figure 2: Schematic pillar diagrams showing (a) pillar and base in titanium alloy and mounted on the test frame with cyanoacrylate-based glue substrate, (b) A2 crystal orientation expected to activate basal slip, and (c) A3 crystal orientation for expected prism slip.

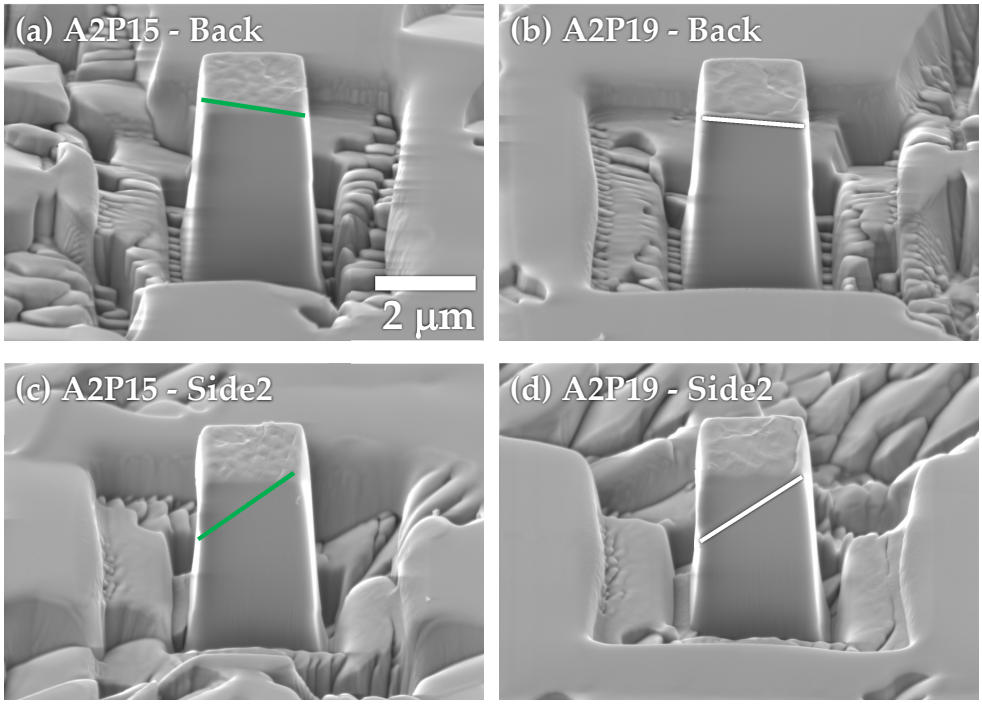


Figure 3: Experimental pillars A2P15 and A2P19 showing (a) and (b) back, and (c) and (d) side views for which the observed basal slip developed is marked by the green and white lines. "Back" and "Side2" views may be identified in Figure 2 (b) and (c).

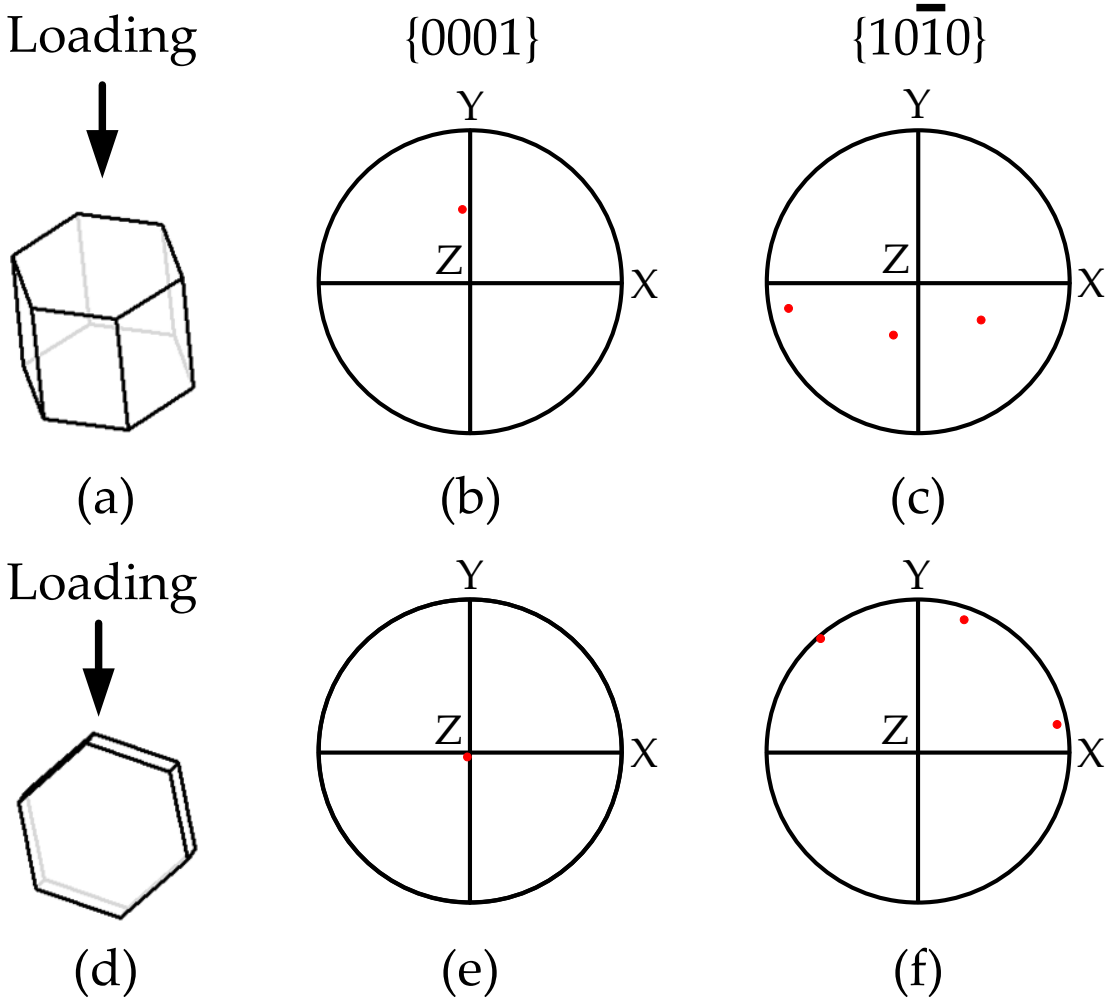


Figure 4: Experimental crystal orientation and pole figures for A2 (basal slip) and A3 (prism slip) pillars: (a) loading with respect to crystal orientation in A2 pillars; (b) and (c) are plane normal pole figures in A2 pillars; (d) loading with respect to crystal orientation in A3 pillars; (e)-(f) are plane normal pole figures in A3 pillars. The loading is in the Y-direction, pillar front and back have normal Z-direction, and the pillar sides have normal in the X-direction, as shown in Figure 2.

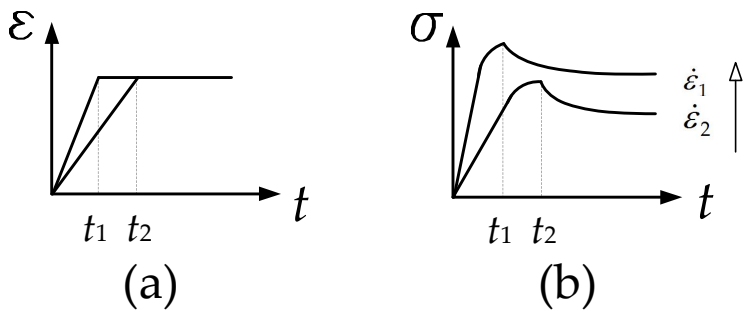


Figure 5: (a) Strain vs time loading at two strain rates and (b) schematic stress vs time anticipated response.

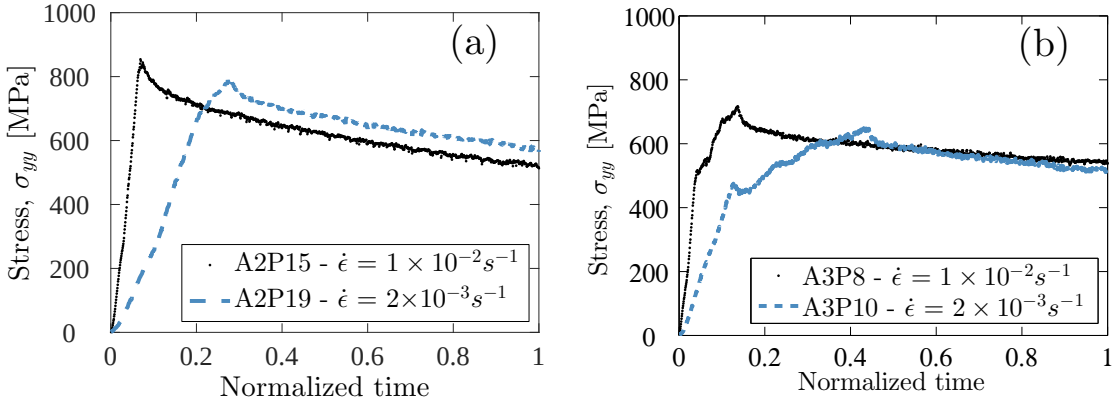


Figure 6: Experimental nominal stress vs (normalized) time graphs for (a) A2 basal slip pillars tested to 5% compressive strain and (b) A3 prism slip pillars tested to 10% compressive strain. The time axis is normalized with respect to the total load + displacement hold duration.

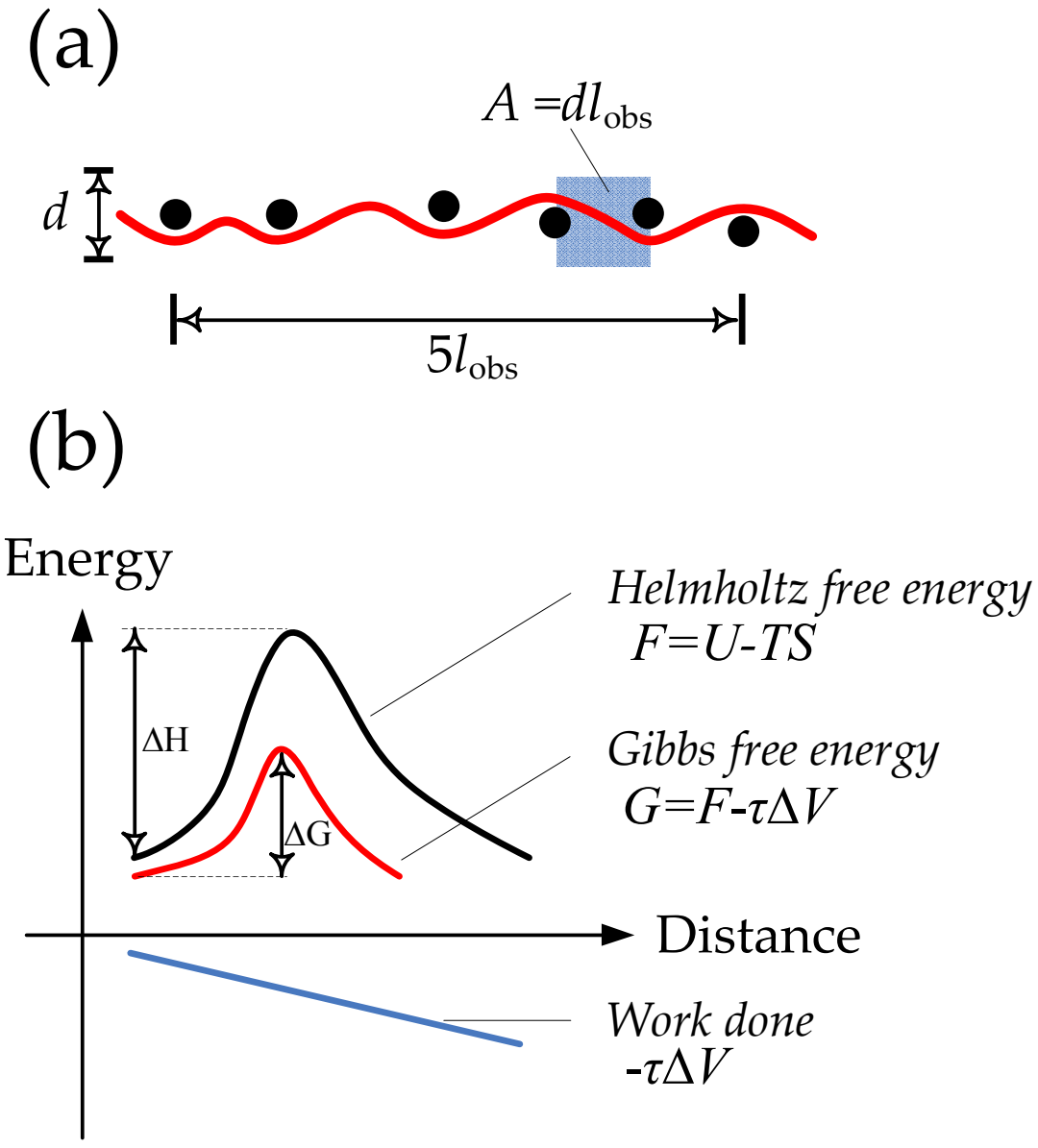


Figure 7: Schematic diagram of (a) a dislocation escaping an obstacle through a thermal activation process and (b) the corresponding energy barrier curves [45]

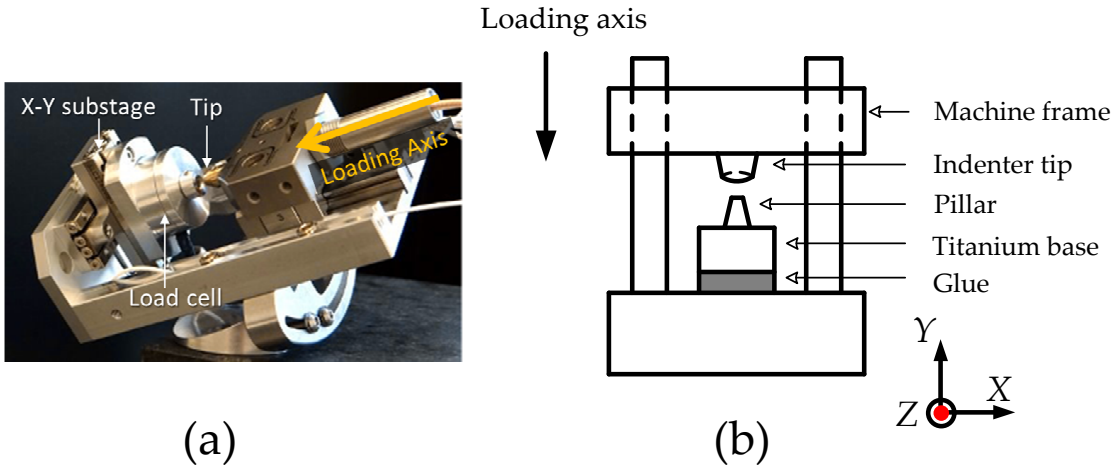


Figure 8: (a) Micro-pillar compression testing setup used in the SEM chamber (b) simplified schematic diagram showing pillar, titanium base, cyanoacrylate-based glue substrate and machine frame.

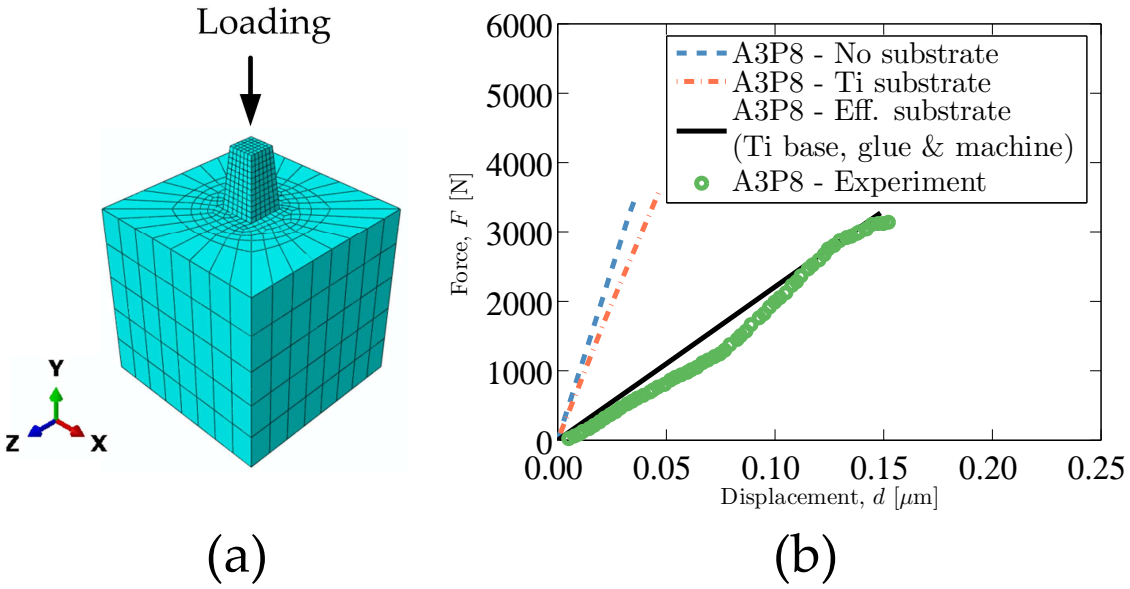


Figure 9: (a) FE pillar model including the effective Ti base under the pillar which is elastically isotropic, and *mechanically equivalent* to Figure 8(b), accounting for the contributions to stiffness from machine loading column, the titanium base, and the glue substrate, and (b) experimentally measured and CPFE calculated force displacement curves for the linear elastic loading phase of the micro-pillar test

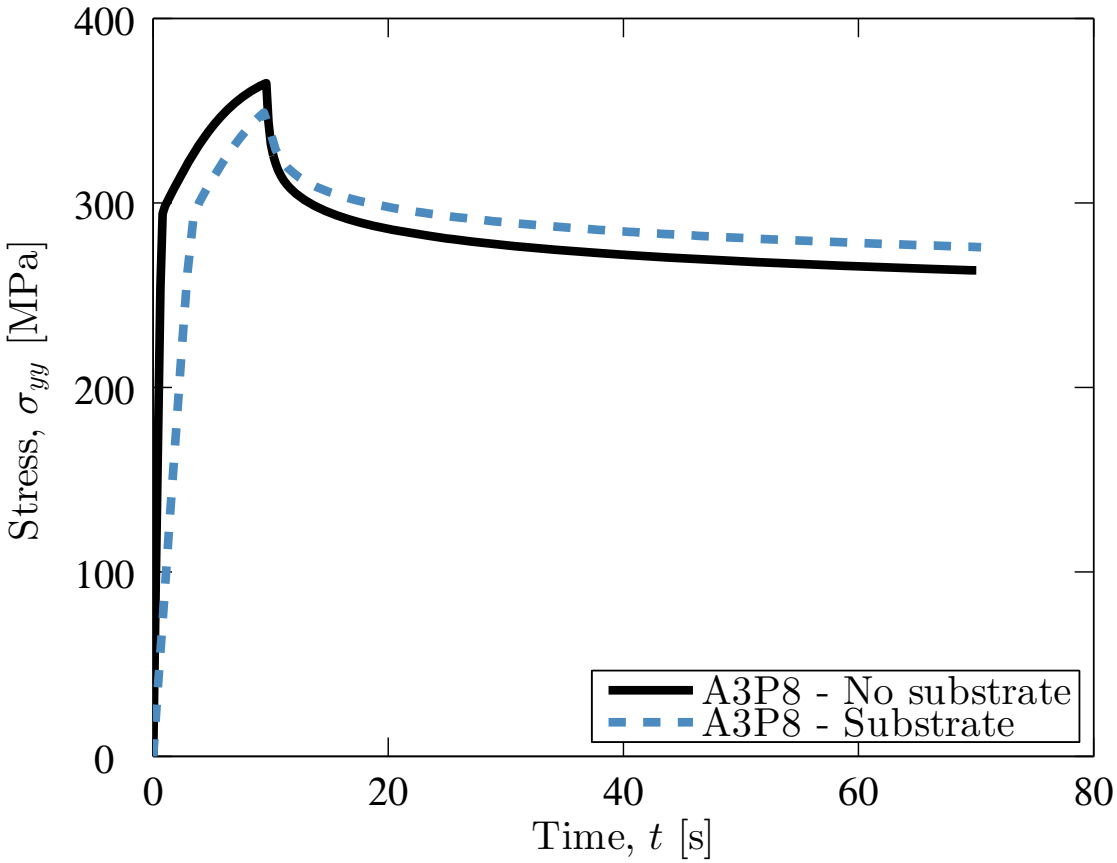


Figure 10: Crystal plasticity finite element model calculations of the effect of including and excluding environmental stiffness (through an effective elastic substrate in Figure 9(a)) on stress response in stress relaxation tests.

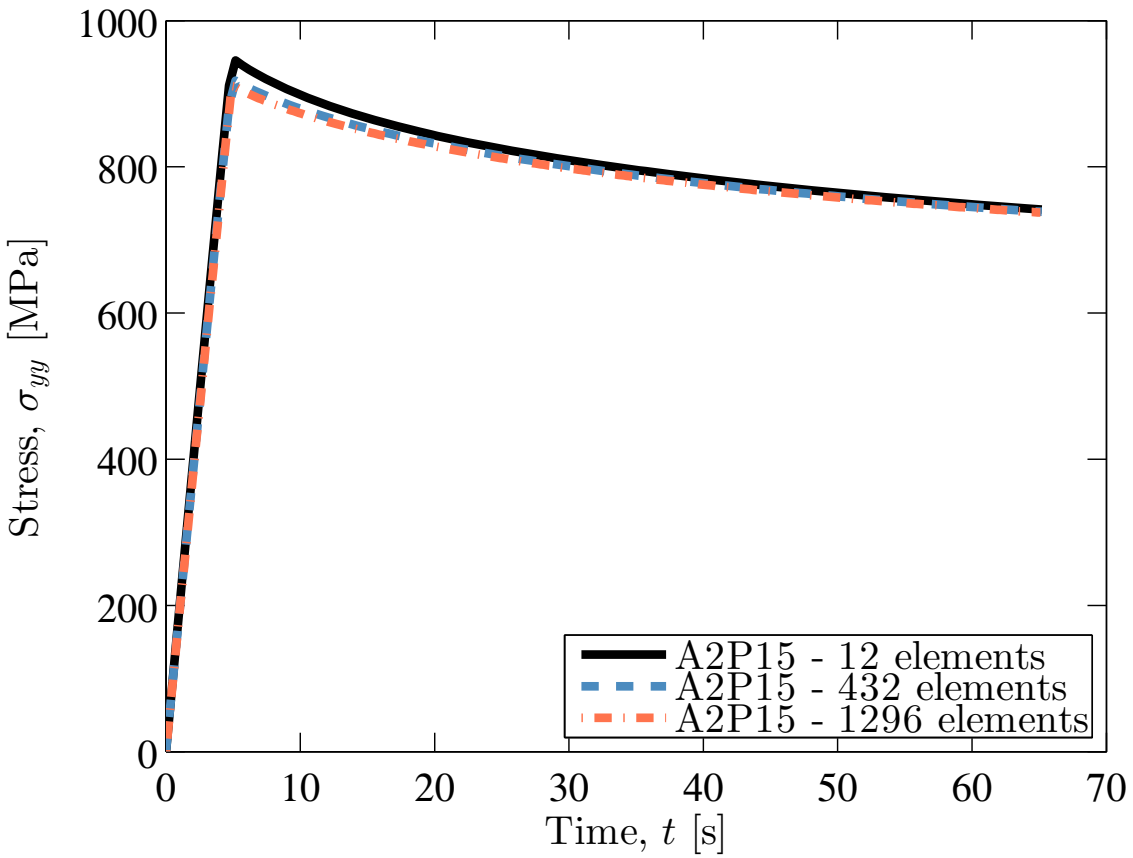


Figure 11: Mesh convergence of micro-pillar compression model with the number of elements within the pillar alone (i.e. excluding base) indicated.

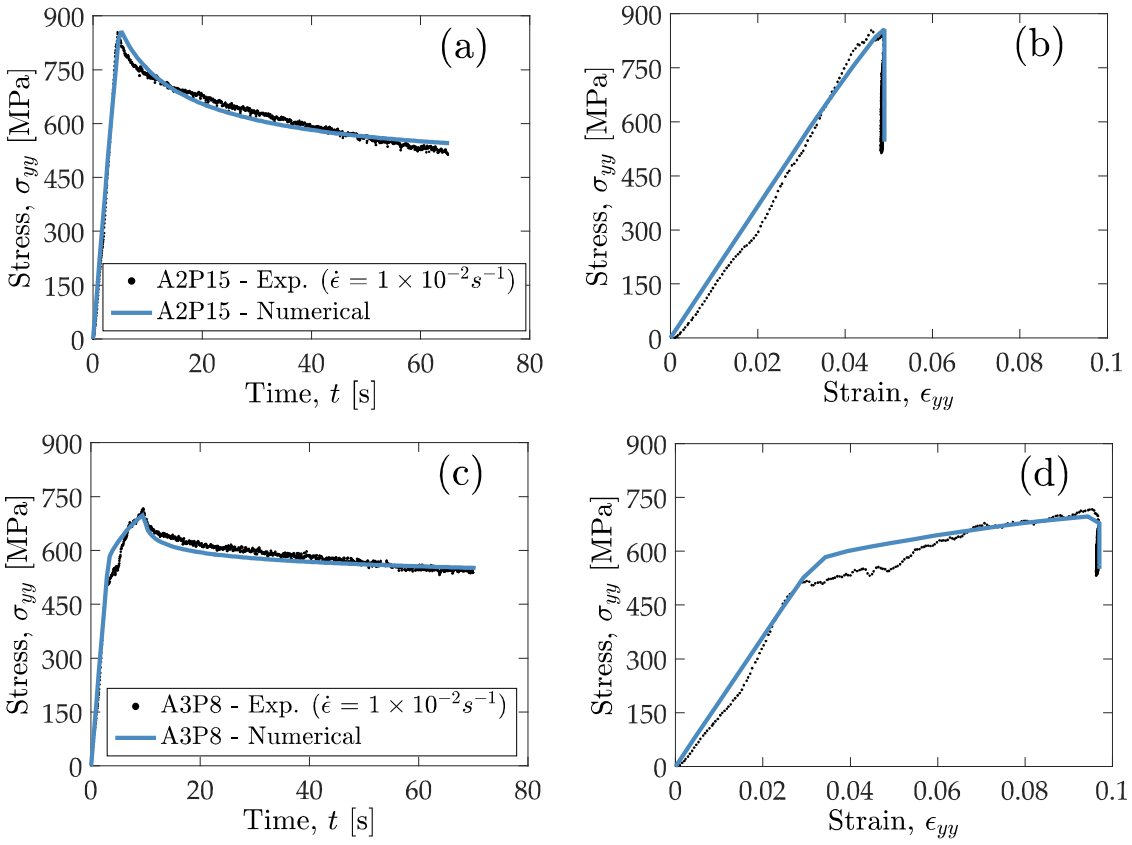


Figure 12: Experimental measured and numerical crystal plasticity calculated results showing (a) stress-time and (b) stress-strain curves in (basal slip) A2P15; (c) stress-time and (d) stress-strain curves in (prism slip) A3P8.

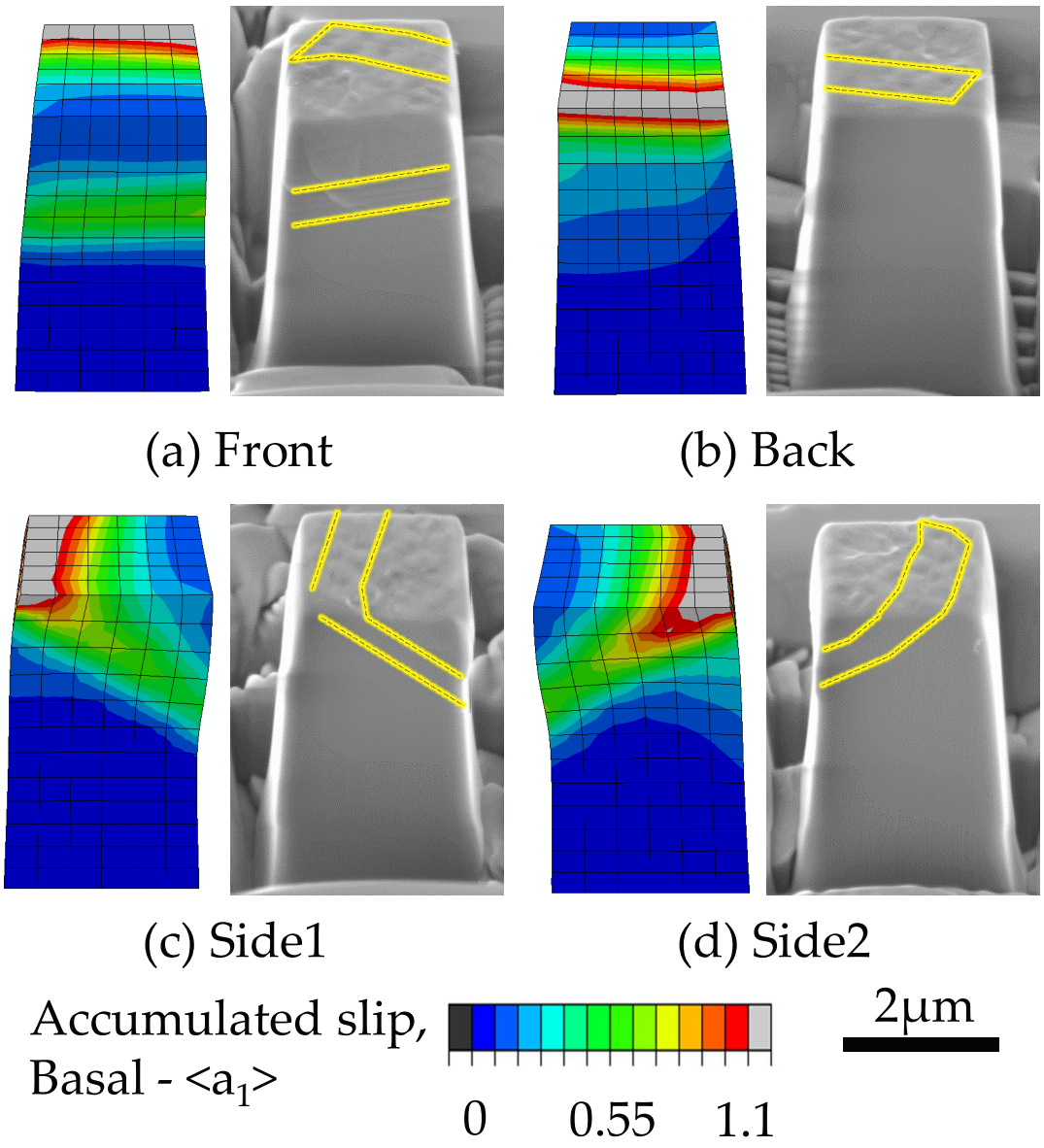


Figure 13: A2P15 micro-pillar tested under strain rate of $1 \times 10^{-2}\ s^{-1}$ showing experimental basal slip $(0001)[\bar{2}110]$ intersecting with four free surfaces of the pillar (right side in (a) to (d)) and predicted results (left side in (a) to (d)).

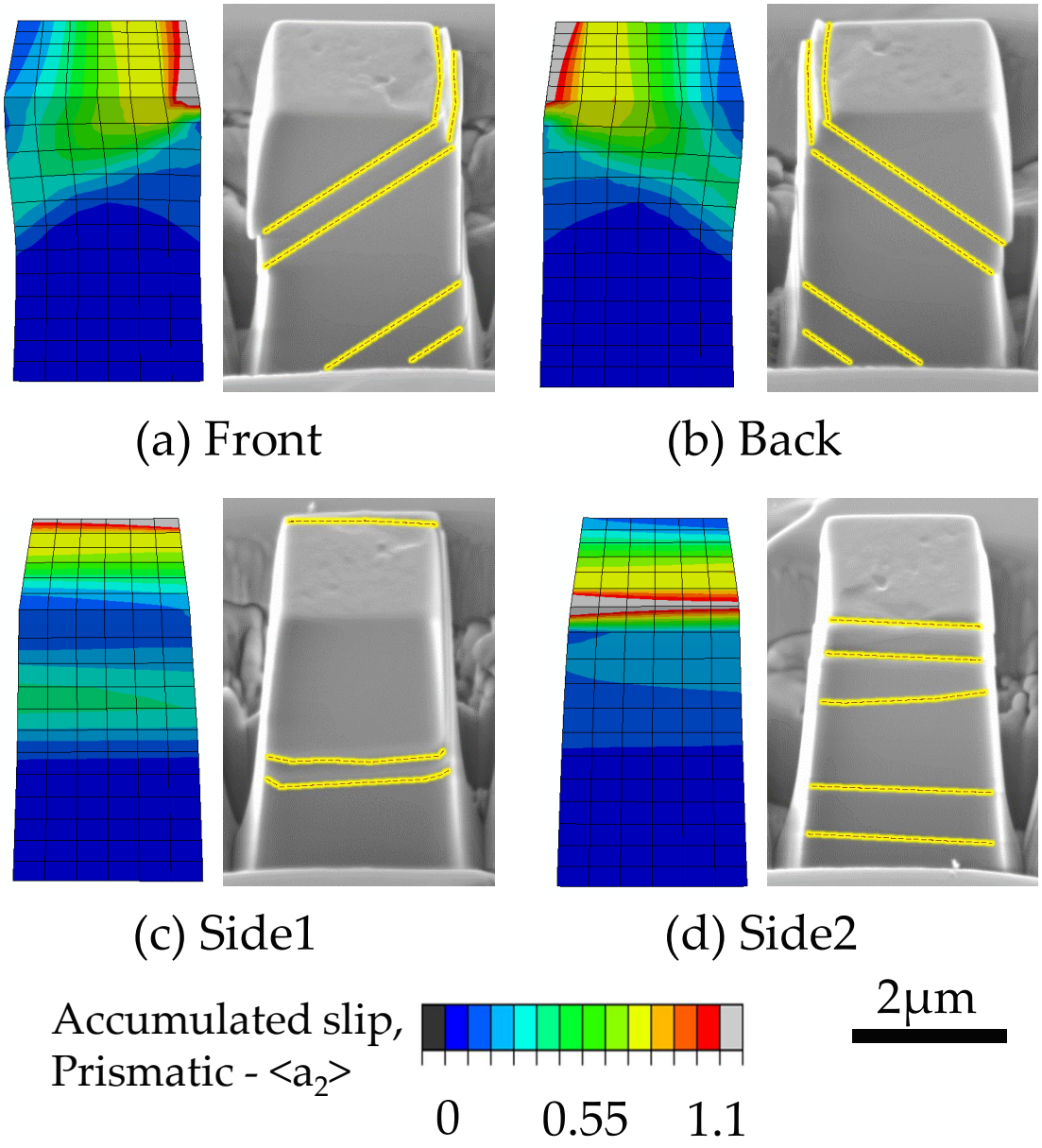


Figure 14: A3P8 micro-pillar tested under strain rate of $1 \times 10^{-2}\ s^{-1}$ showing experimental prismatic slip $(1010)[\bar{1}2\bar{1}0]$ intersecting with four free surfaces of the pillar (right side in (a) to (d)) and predicted results (left side in (a) to (d)).

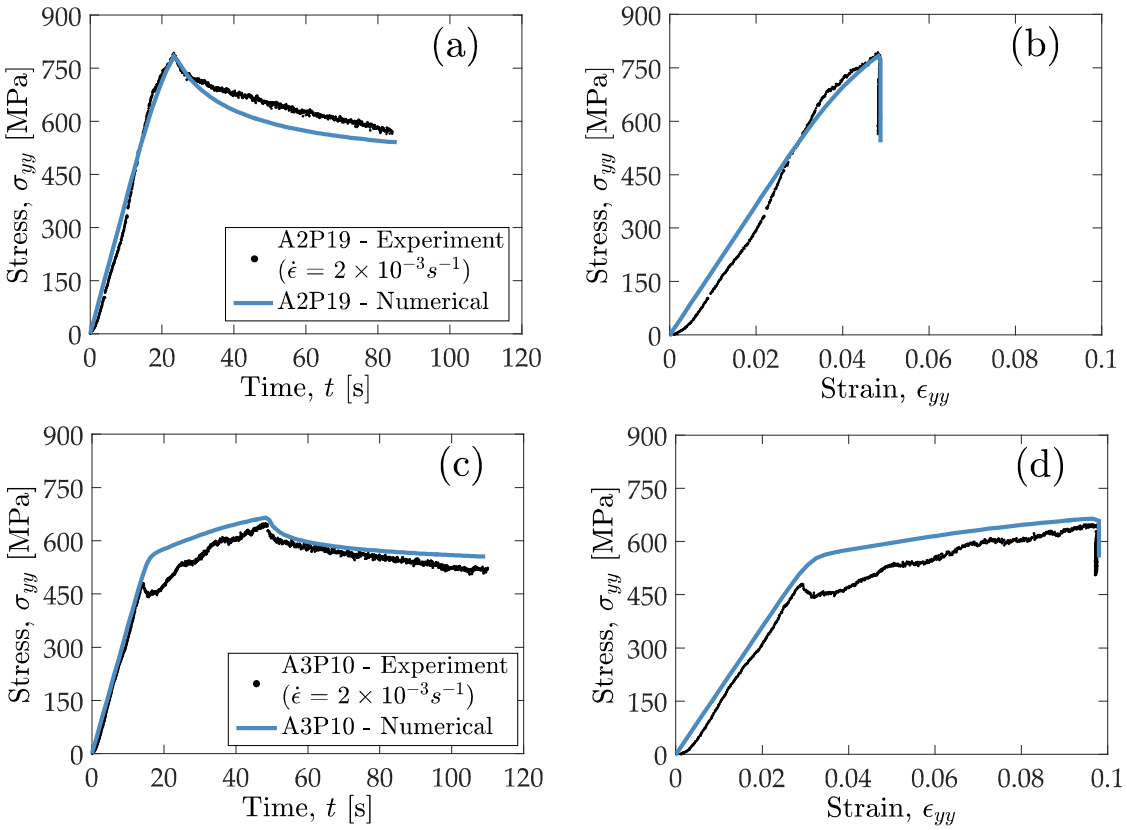


Figure 15: Experimental measured and blind prediction of numerical crystal plasticity calculated results showing (a) stress-time and (b) stress-strain curves in (basal slip) A2P19; (c) stress-time and (d) stress-strain curves in (prism slip) A3P10.

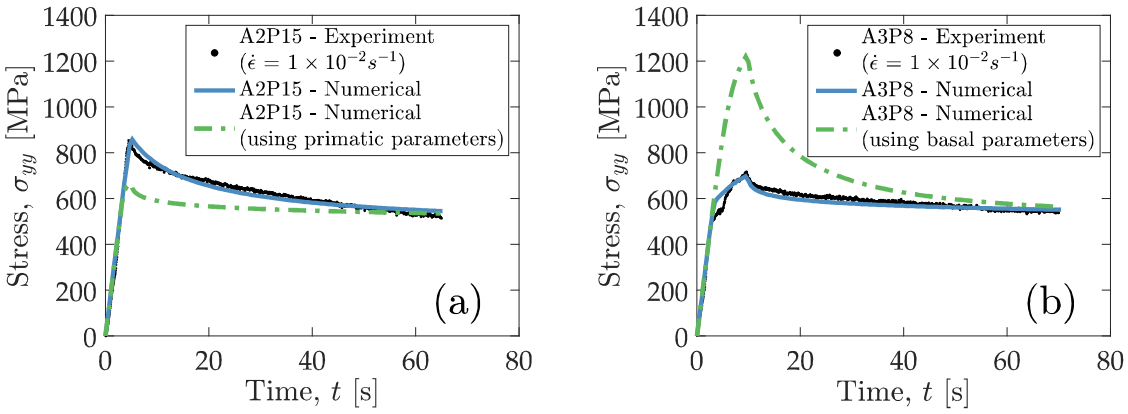


Figure 16: Sensitivity study showing original experimental and predicted stress relaxation response for (a) the basal slip pillar and (b) the prismatic slip pillar but showing also (in broken green) the predicted responses if the rate-sensitivity properties for basal and prism slip are exchanged in the model.